



Effect of energy input on formability, microstructure and mechanical properties of selective laser melted AZ91D magnesium alloy



Kaiwen Wei, Ming Gao*, Zemin Wang, Xiaoyan Zeng

Wuhan National Laboratory for Optoelectronics, Huazhong University of Science and Technology, Wuhan 430074, China

ARTICLE INFO

Article history:

Received 24 December 2013

Received in revised form

13 May 2014

Accepted 30 May 2014

Available online 9 June 2014

Keywords:

Selective laser melting

AZ91D

Formability

Microstructure

Mechanical property

ABSTRACT

Selective laser melting (SLM) technology has been used to manufacture the AZ91D magnesium alloy. The relative density, microstructure, microhardness and tensile properties of the deposited AZ91D samples at different laser energy inputs were characterized. The results indicate that laser energy input plays a significant role in determining formation qualities of the SLMed samples. High density samples without obvious macro-defects can be obtained between 83 J/mm³ and 167 J/mm³. The SLMed AZ91D presents a unique layerwise feature in which the fully divorced eutectic β -Mg₁₇Al₁₂ distributing along the boundary of the equiaxed α -Mg matrix. The average size of α -Mg in overlapping regions is a little larger than that in the center of the scanning tracks due to the remelting process though the element distributions of Mg and Al are quite uniform. The microhardness of all samples shows directional independence. The microhardness and tensile strengths of the SLMed AZ91D at room temperature are superior to those of the die-cast AZ91D due to the combined effect of grain refinement and solid solution strengthening.

© 2014 Elsevier B.V. All rights reserved.

1. Introduction

As the lightest structural alloys, magnesium alloys have the potential to replace steels and aluminum alloys in many applications due to their high specific strength and excellent damping capacity. For example, magnesium alloys are excellent candidates for automotive and aerospace components to reduce weight and realize fuel conservation and emission reduction [1,2]. Besides, in medical field, surgical implants based on magnesium alloys have become a promising invention due to their good degradability in situ and elasticity moduli closer to human bone than other conventional materials [3,4].

The manufacturing methods of magnesium alloys have been paid more attentions to meet the increasing applications. Deformation processing and casting are two conventional methods to manufacture complex magnesium alloy parts. In industry, deformation processing is preferred to obtain metal parts with high performances. However, for magnesium alloys, only two effective slip systems are available at room temperature due to the nature of close-packed hexagonal structure. Deformation processing of magnesium alloys needs to be conducted at elevated temperatures, which causes more fuel consumption, lower efficiency and oxidation of parts. As a result, the consumption of wrought magnesium alloys is merely about 1.5% of total magnesium alloy

demands [5]. At present, die-casting is the dominate method to manufacture magnesium alloys. Although die-casting is of great efficiency together with high precision, gas entrapment is inevitable due to the high filling rates [1,6]. Moreover, complex structures such as internal channels, curved surfaces and ultrafine lattices, are difficult to manufacture by die-casting though their increasing needs in automobiles and surgical implants. Thus, although much of growth is in the area of die-cast parts, new manufacturing methods are still urgently being developed to promote further applications of magnesium alloys.

Selective laser melting (SLM) is one of the most promising laser-assisted additive manufacturing methods that can fabricate near net shape components according to CAD model without any tools or molds in a relatively short cycle [7,8]. With the aid of additive support structures and unirradiated powders, SLM technology has the capability to build any complex shape of metal parts that would otherwise be difficult or impossible to produce using conventional manufacturing methods. On the other hand, small molten pools and heat affected zones are induced by the fast scanning laser beam under the control of the galvanometer, which generates high cooling rates of 10^3 – 10^4 K/s inside the molten pools [9,10]. Such high cooling rates may lead to the refinement of microstructure and help to improve essential performances of parts needed in automotive industry and medical implantation. In summary, SLM is an effective way to expand the applied range of magnesium alloys further.

So far, only a few researches on processing pure magnesium or its mixtures using SLM have been reported. Ng et al. [11] have

* Corresponding author. Tel.: +86 27 87792404.

E-mail address: mgao@hust.edu.cn (M. Gao).

studied the single-track formation of pure magnesium using a home-developed SLM system. They found that the width and height of a single track are almost consistent though the laser energy changes. However, there was no attempt to manufacture the more meaningful three-dimensional components. Zhang et al. [12] successfully obtained a SLM parameter window to process the mixture of pure magnesium and pure aluminum with a weight ratio of 91:9. However, the deposited samples only have a highest relative density of 82% and no data about the mechanical properties are given. Obviously, above studies demonstrate that SLM technology is a promising method to develop magnesium or its alloys. Compared with pure magnesium and magnesium-

aluminum mixtures, commercial magnesium alloys have more important application value in industry and medical area. But no reports have been presented to explain the deposition mechanism, formability, microstructure and mechanical properties of SLMed magnesium alloys despite their importance to further applications.

As one of the Mg-Al-Zn (AZ) alloys, AZ91D is a widely used cast magnesium alloy with excellent comprehensive performance. For example, AZ91D is often used as the material of transmission parts in automobile industry and porous implants in medical domain. AZ91D parts with complex structures and high performance are increasing fast in number to challenge conventional manufacturing methods. SLM technique can be used to solve the above manufacturing problems efficiently only after the basic knowledge has been made clear. Therefore, AZ91D is processed by SLM in this study. Forming ability of AZ91D as well as relationship of laser energy input with microstructure and mechanical properties have been studied. Finally, high-density AZ91D parts with better mechanical strengths than conventional die-cast ones are obtained.

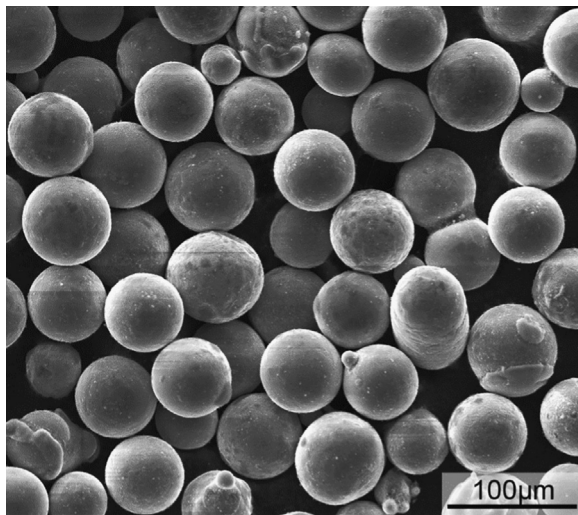


Fig. 1. SEM image showing characteristic morphology of AZ91D powders.

Table 1
Chemical compositions of AZ91D and AZ31B (wt%).

	Al	Zn	Mn	Mg
AZ91D	8.95	0.44	0.19	Bal.
AZ31B	3.34	0.61	0.29	Bal.

2. Experimental procedures

Spherical gas atomized AZ91D powders with a mean particle size of 59 μm and an apparent density of 0.95 g/cm^3 were used as the starting material in SLM experiments, whose morphology is shown in Fig. 1. A commercial die-cast AZ91D ingot with the same composition was also prepared for comparison. Rolled AZ31B plates with a thickness of 35 mm were used as the substrate plates. The chemical compositions of AZ91D and AZ31B used in experiments are listed in Table 1.

All the samples were built by a self-developed SLM system (LSNF-I). Details about the SLM system has been described in our previous publications [13,14], and they will be introduced briefly here. The SLM machine mainly consists of a continuous wave IPG YLR-200 fiber laser ($\lambda = 1.07 \mu\text{m}$), an automatic powder delivery system, a building platform, and a computer system for process control. The manufacturing software controls the movements of the scanner, recoater, powder dispenser and building platform to fabricate parts according to the 3D model. All the SLM experiments were conducted in an argon atmosphere with the concentrations of H_2O and O_2 both controlled below 50 ppm. In addition, a

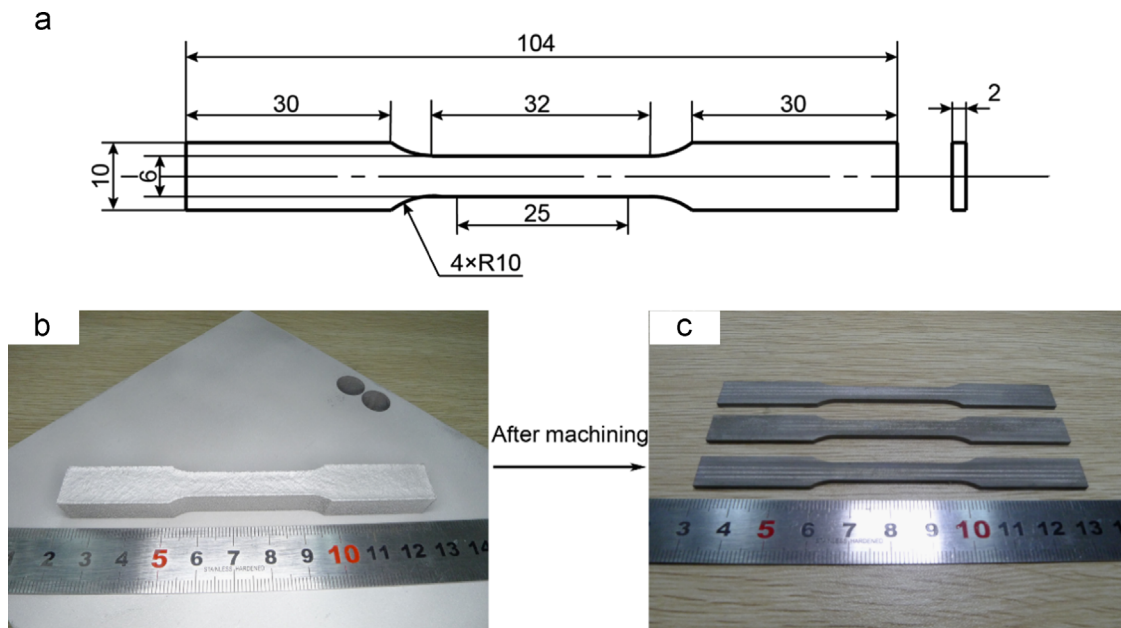


Fig. 2. SLMed AZ91D tensile testpieces in this study. (a) Configuration, (b) SLMed part, (c) tensile testpieces.

standard alternating x/y raster strategy was chosen for laser scanning paths. This strategy features bidirectional hatches of a layer ' n ' performed in x -direction whilst the next layer ' $n+1$ ' turned 90° .

Microstructures of the SLMed samples were observed by standard metallographic techniques using an optical microscopy (Nikon EPIPHOT 300). Phase structure of deposited layers was checked by X-ray diffraction (PANalytical X'Pert PRO) with Cu K α radiation. Surface appearances and microstructures of the samples were characterized by a scanning electron microscopy (FEI Nova NanoSEM 450). The distribution of chemical composition was examined by an energy dispersive spectroscopy (Oxford X-Max 50). Microhardness tests were carried out using an HVS-1000 microhardness tester at a load of 200 g and a holding time of 15 s. As shown in Fig. 2, tensile testpieces were first designed according to the ASTM B557M-10 standard. Then several series of standard AZ91D tensile testpieces manufactured at different laser energy inputs were machined and examined using a Zwick/Roell tester at room temperature. After tensile tests, fracture faces were characterized by the scanning electron microscopy.

Table 2
SLM manufacturing parameters used in this study.

Manufacturing parameters	Value
Laser power P , W	200
Scanning velocity V , m/min	10, 20, 30, 40, 50 and 60
Layer thickness T , mm	0.04
Hatch spacing S , mm	0.07, 0.09, 0.11 and 0.13

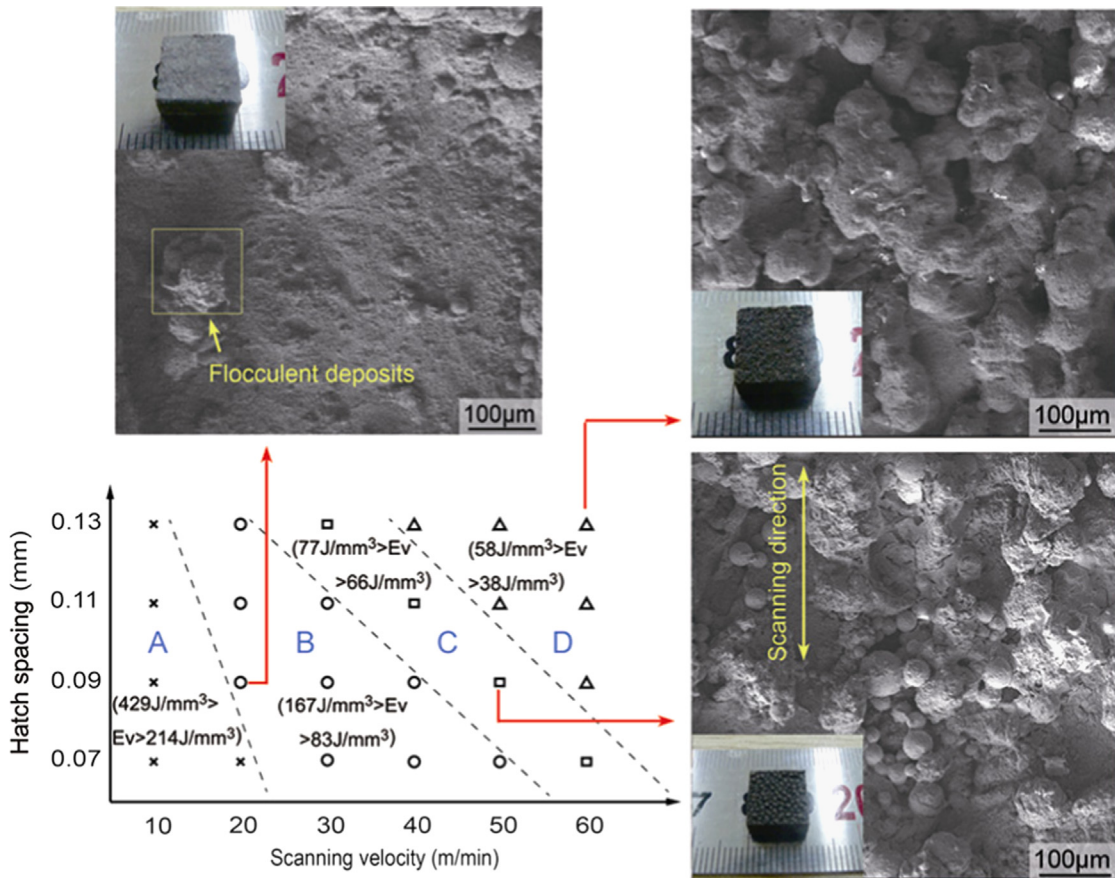


Fig. 3. The processing map of SLM experiments based on laser energy input.

3. Results and discussion

3.1. Formability

During SLM experiments, 24 cubic samples with a size of $10 \times 10 \times 5$ mm 3 were first built to optimize the SLM parameters. Parameters used in this study are presented in Table 2. A processing map based on the formability of AZ91D magnesium alloy powders was then established, as shown in Fig. 3. It could be found that the formability of AZ91D during SLM process directly depends on the input of laser energy. Considering the thickness of powder layer, the input of laser energy during fabrication can be represented better by the volume energy density E_v . Here volume energy density E_v is defined as the laser energy per volume and can be calculated by the following equation:

$$E_v = \frac{P}{STV} \quad (1)$$

where P is the laser power, S is the hatch spacing, T is the layer thickness and V is the scanning velocity.

Based on the calculation of Eq. (1) at different parameter combinations, the processing map in Fig. 3 can be divided into four zones. In zone A, high energy inputs with E_v above 214 J/mm 3 make the temperature in the molten pools increase too much, which causes serious evaporation of the powders due to low boiling point and high vapor pressure of magnesium. The evaporated powders expand rapidly and exert a high recoil pressure on the molten pools. Molten pools together with the surrounding unmelted powders are then blown away to make the SLM process failure. In zone B, AZ91D samples without obvious macro-defects are built in a proper range of E_v between 83 J/mm 3 and 167 J/mm 3 .

However, flocculent depositions together with distorted scanning tracks caused by the evaporation of metal powders can still be found on the surface of sample fabricated at 166.7 J/mm^3 . In zone C, where E_v is in the range of 66 J/mm^3 to 77 J/mm^3 , “balling effect” arises on the surface of SLMed samples. Molten pools with small circumference-to-length ratios generated at relatively low energy inputs are unstable. As described by Yadroitsev et al. [7], scanning tracks decompose into discrete droplets in this condition. Thus, ball-like particles parallel to scanning direction together with large quantities of unmelted powders induce a more deteriorated surface, which can be observed from the fabricated sample at 66.7 J/mm^3 . Finally, in zone D, where E_v is below 58 J/mm^3 , loose samples without mechanical strength are obtained due to incomplete melt of most of the powders.

In order to further understand how the energy input influences formability, relative density of the deposited AZ91D samples was analyzed by measuring the porosity. According to quantitative stereology, the porosity of sample is considered to be equivalent to the area percentage of pores in tested sections [15]. An Image-Pro Plus 6.0 software was utilized to analyze the porosity. First, for each SLMed sample, two sections parallel to deposition direction were taken into account. For each section, after grinding and polishing, optical micrographs of four random selected positions were taken at a magnification of $50\times$. Second, all the micrographs were transformed into the gray mode and a proper threshold value of grayscale was chosen using the segmentation function of the software to mark regions where the grayscale is the same as the pores. Third, the area percentage of pores in each micrograph was determined by calculating the area ratio of the marked regions to the whole micrograph with the help of the statistics function. Finally, the porosity of each SLMed sample was determined by counting the average area percentage of pores based on the eight optical micrographs. Fig. 4 gives the relationship between the relative density and scanning velocity at different hatch spacings. There is a general decreasing trend of the relative density with increasing scanning velocity for all hatch spacings, which demonstrates that the relative density of SLMed samples is decided by the energy input. During SLM process, relatively high E_v induced by slow scanning velocities leads to a sufficient irradiation time. Thus, powders are fully melted and the gas entrapped or generated in the molten pool has enough time to release. On the contrary, short irradiation time induced by relative high scanning velocities results in partial melt of powders and serious entrapment of gas. Thus, poor bond of adjacent scanning

tracks leads to the decrease in relative density. In the present study, the highest relative density of SLMed AZ91D sample is 99.52% at E_v of 166.7 J/mm^3 ($P=200 \text{ W}$, $S=0.09 \text{ mm}$, $T=0.04 \text{ mm}$, $V=20 \text{ m/min}$). Relative density may influence mechanical properties of the SLMed samples and this will be discussed in the subsequent sections.

3.2. Microstructure characterization

XRD patterns of the SLMed samples built at different energy inputs are shown in Fig. 5a. It is evident that samples are all composed of $\alpha\text{-Mg}$, $\beta\text{-Mg}_{17}\text{Al}_{12}$ and a lesser degree of Al_8Mn_5 . No peaks corresponding to MgO and Al_2O_3 are found due to strict control of the concentrations of H_2O and O_2 . Through a close-up view of the XRD patterns, as shown in Fig. 5b and c, $\alpha\text{-Mg}$ peaks slightly shift to low diffraction angles with decreasing E_v . Since atomic radii of Al (0.1199 nm) and Zn (0.1187 nm) are 89.95% and 89.05% of Mg (0.1333 nm) [16], Al and Zn act as substitutive solutes in the $\alpha\text{-Mg}$ matrix according to the theory of solid solution. When E_v decreases from 166.7 J/mm^3 to 66.7 J/mm^3 , temperatures of the molten pools reduce and the evaporation of Mg element becomes weak, which results in decrease of contents of Al and Zn in $\alpha\text{-Mg}$ matrix. Therefore, lattice parameters of $\alpha\text{-Mg}$ become larger and $\alpha\text{-Mg}$ diffraction peaks shift to low angles. Table 3 lists intensity ratios of major peaks of $\beta\text{-Mg}_{17}\text{Al}_{12}$ to $\alpha\text{-Mg}$ phase at different energy inputs. Note that β phase becomes less with decreasing energy input and this phenomenon will be discussed further in subsequent chapter.

Fig. 6 presents the optical micrographs of the AZ91D sample deposited at 166.7 J/mm^3 . In Fig. 6a, molten pools with elliptical bottom induced by the Gaussian distribution of laser energy align layer by layer, which shows a layerwise feature intrinsic to SLM technology. All the ends of melted tracks are close stacked to form a good metallurgical bonding between two neighbor layers though several micropores still exist. In Fig. 6b, it is easy to find that the penetration depth of molten pools can be up to $312 \mu\text{m}$, which is approximately eight times the layer thickness. Therefore, except for the last layer, each layer of the as-deposited sample undergoes remelting process more than once. Multiple remelting processes not only help to improve the quality of metallurgical bond between neighbor tracks and layers, but also play a significant role in determining the microstructure of SLMed samples. From Fig. 6c, close stacked scanning tracks can be seen in the cross section. It is necessary to point out that discontinuous scanning tracks from different layers can also be observed due to the fluctuation of molten pools and the alternating raster filling strategy. Fig. 6d gives the detail of scanning tracks shown in Fig. 6c and it is quite apparent that the microstructure is not uniform. During SLM process, in order to acquire metallurgical bond with high quality, hatch spacing between two neighbor tracks should be smaller than the track width. As shown in Fig. 6d, the overlap regions between two neighbor tracks are defined as the overlapping regions (hereafter called OLR) whilst other regions are defined as the center of scanning tracks (hereafter called CST). The difference in thermal history between OLR and CST induces the nonuniform microstructure of the deposited AZ91D samples.

SEM micrographs of SLMed AZ91D at the energy input of 166.7 J/mm^3 are shown in Fig. 7a and b. The microstructure presents a feature of equiaxed $\alpha\text{-Mg}$ with fully divorced eutectic $\beta\text{-Mg}_{17}\text{Al}_{12}$ distributing reticularly along the boundary. Although Al_8Mn_5 are believed to exist according to XRD patterns, they are not found throughout the micrographs due to the very low content. Grain sizes of $\alpha\text{-Mg}$ matrix are quite fine due to the high cooling rates of SLM. From Fig. 7c and d, the average grain size of $\alpha\text{-Mg}$ in CST and OLR are measured to be $1.0 \mu\text{m}$ and $2.9 \mu\text{m}$,

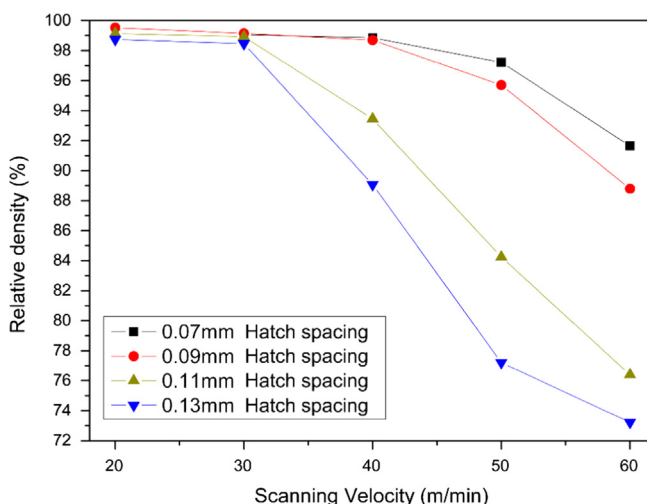


Fig. 4. Relative density of the SLMed samples deposited at different SLM parameters.

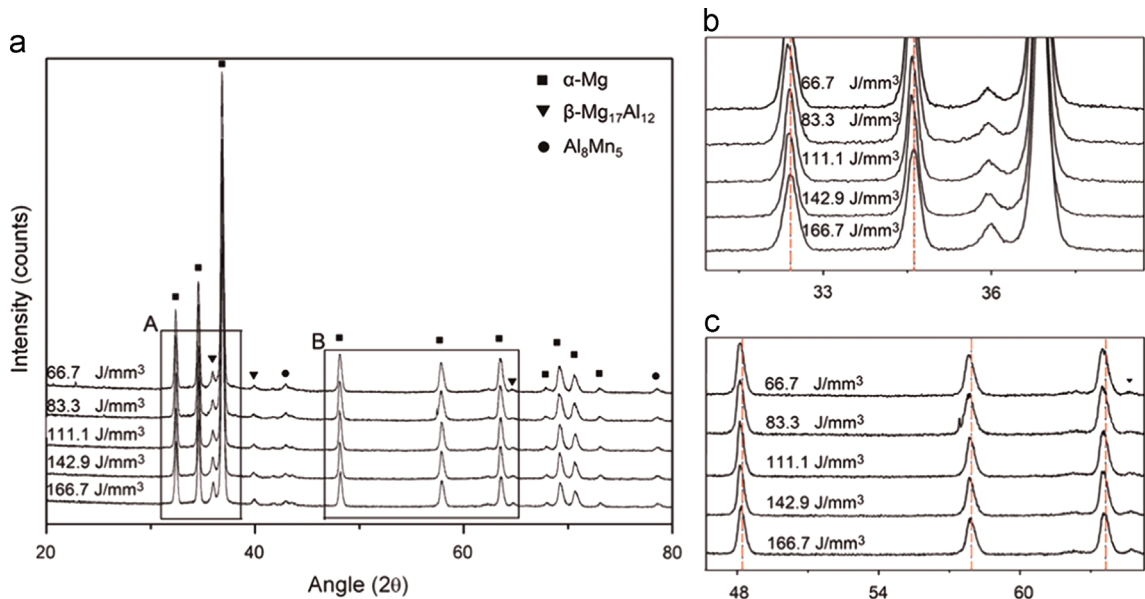


Fig. 5. (a) XRD patterns of the SLMed samples at different E_v , (b) and (c) details about regions marked as A and B shown in (a).

Table 3

Intensity ratios of major X-ray diffraction peaks of β and α phase, I_β/I_α , as measured in the deposited samples at different E_v .

I_β/I_α (%)	As-deposited samples at different E_v				
	166.7 J/mm ³	142.9 J/mm ³	111.1 J/mm ³	83.3 J/mm ³	66.7 J/mm ³
Intensity ratio of (411) peak of β phase to (101) peak of α phase	6.02	5.78	5.04	4.81	3.84
Intensity ratio of (332) peak of β phase to (101) peak of α phase	2.21	1.90	1.98	2.06	1.20

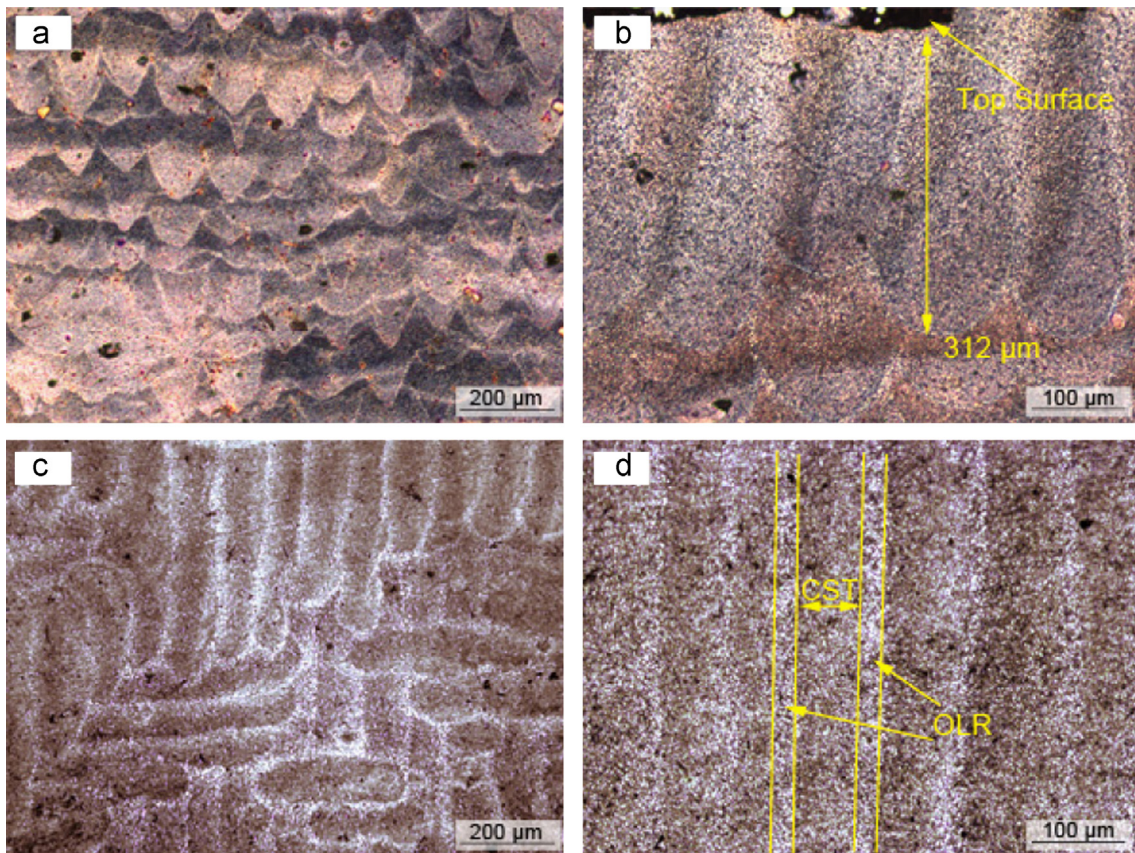


Fig. 6. Optical micrographs of the AZ91D sample deposited at E_v of 166.7 J/mm³. (a) and (b) The vertical section, (c) the cross section, and (d) the detail of scanning tracks shown in (c).

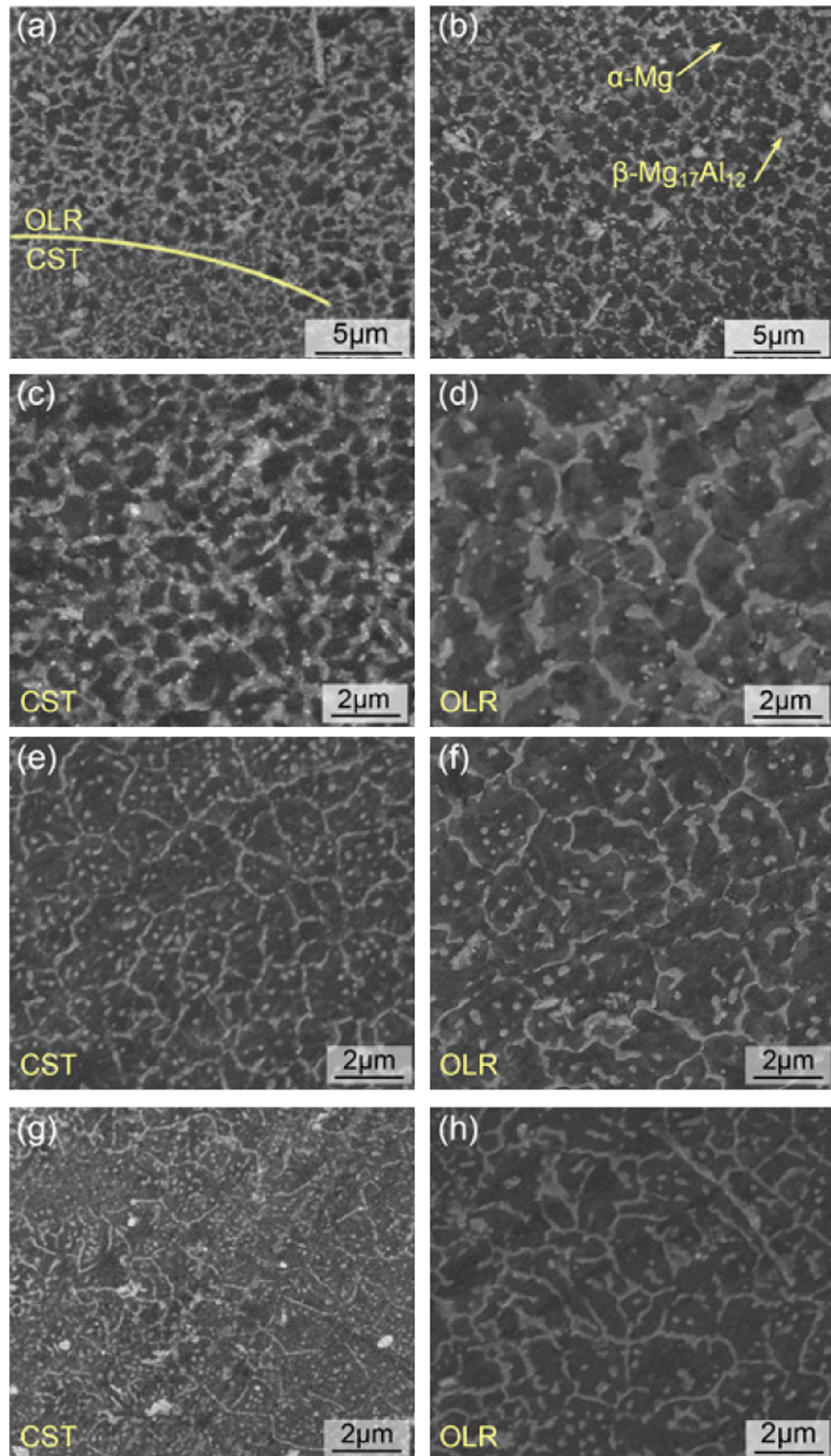


Fig. 7. SEM micrographs of AZ91D samples built at different E_v . (a) The cross section of the sample built at 166.7 J/mm³, (b) the vertical section of the sample built at 166.7 J/mm³, (c) details of CST in (a), (d) details of OLR in (a), (e) and (f) CST and OLR in the cross section of the sample built at 111.1 J/mm³, (g) and (h) CST and OLR in the cross section of the sample built at 83.3 J/mm³.

respectively. Compared with CST, OLR experiences more cycles of remelting process to induce relatively lower cooling rates, which causes the microstructures in OLR coarsen. This phenomenon has also been found by Guan et al. [17] during laser surface melting of

AZ91D. However, this kind of nonuniform distribution of microstructure is in the scale of several microns, which may only lead to the mechanical performance like microhardness fluctuates in a smaller range.

SEM micrographs of samples deposited at 111.1 J/mm³ and 83.3 J/mm³ are also presented in Fig. 7e, f, g and h. The coarsening of microstructures in OLR is observed again. Moreover, β phase becomes lesser and thinner both in OLR and CST with decreasing E_v , which is totally consistent with the variation in intensity ratio of major diffraction peaks of β to α phase shown in Table 3. There may be two reasons to explain this phenomenon. One is lower E_v reduces the evaporation capacity of Mg and then $\beta\text{-Mg}_{17}\text{Al}_{12}$ which is enrichment of Al becomes less with decreasing content of Al. Another reason can be explained by the effect of “solute capture”. According to the model for solute redistribution during continuous growth in rapid solidification established by Aziz [18], solute distribution coefficient of the moving solid–liquid phase interface (k_v) can be calculated by the following formula:

$$k_v = \frac{k_e + R/V_d}{1 + R/V_d} \quad (2)$$

where k_e is the equilibrium segregation coefficient, R is the growth rate of the solid/liquid interface and V_d is the diffusive speed of a solute atom at the interface. From the above formula, k_v is not a constant but a dynamics-dependent variable which changes monotonously from k_e to 1 with the increase of R from 0 to ∞ . During SLM process, R is directly proportional to the scanning velocity V . Under the control of the galvanometer, the scanning velocity adopted in this study is as high as tens of meters per minute, which results in the rapid motion of the solid/liquid

interface. Thus, during solidification of the deposited layers, k_v is considerably larger than k_e and the condition of local equilibrium near the interface is significantly deviated. The diffusion time of Al is insufficient so that “solute capture” phenomenon in the $\alpha\text{-Mg}$ matrix appears and therefore, the formation of Al-rich β phase is inhibited to some extent. By lowering down the energy input from 166.7 J/mm³ to 83.3 J/mm³, in other words, by increasing the scanning velocity from 20 m/min to 40 m/min, the growth rate of the interface R increases to a much higher degree. Therefore, k_v further approaches to 1 and a higher proportion of solute atom is captured in the matrix $\alpha\text{-Mg}$ to further retard the nucleation of $\beta\text{-Mg}_{17}\text{Al}_{12}$.

For comparison, the microstructure of commercial die-cast AZ91D is presented in Fig. 8a and b. The die-cast ingot is also composed of $\alpha\text{-Mg}$ solid solution and $\beta\text{-Mg}_{17}\text{Al}_{12}$ eutectic phase distributing along the grain boundaries. From the magnified micrograph of region A (inset in Fig. 8b), it could be found that some bulky divorced eutectic $\beta\text{-Mg}_{17}\text{Al}_{12}$ are surrounded by the lamellar eutectic. The lamellar structure is believed to form through the cellular growth of alternating plates of the $\beta\text{-Mg}_{17}\text{Al}_{12}$ phase and the $\alpha\text{-Mg}$ phase at high angle boundaries [19]. Thus, in the die-cast AZ91D ingot, β precipitates exist in the form of partially divorced eutectic structure. AZ91D is approximately one of the hypoeutectic Mg-Al alloys due to its low content of Zn. According to Dahle's report [20], the morphology of eutectic in the hypoeutectic Mg-Al alloys depends on the cooling rate. The higher

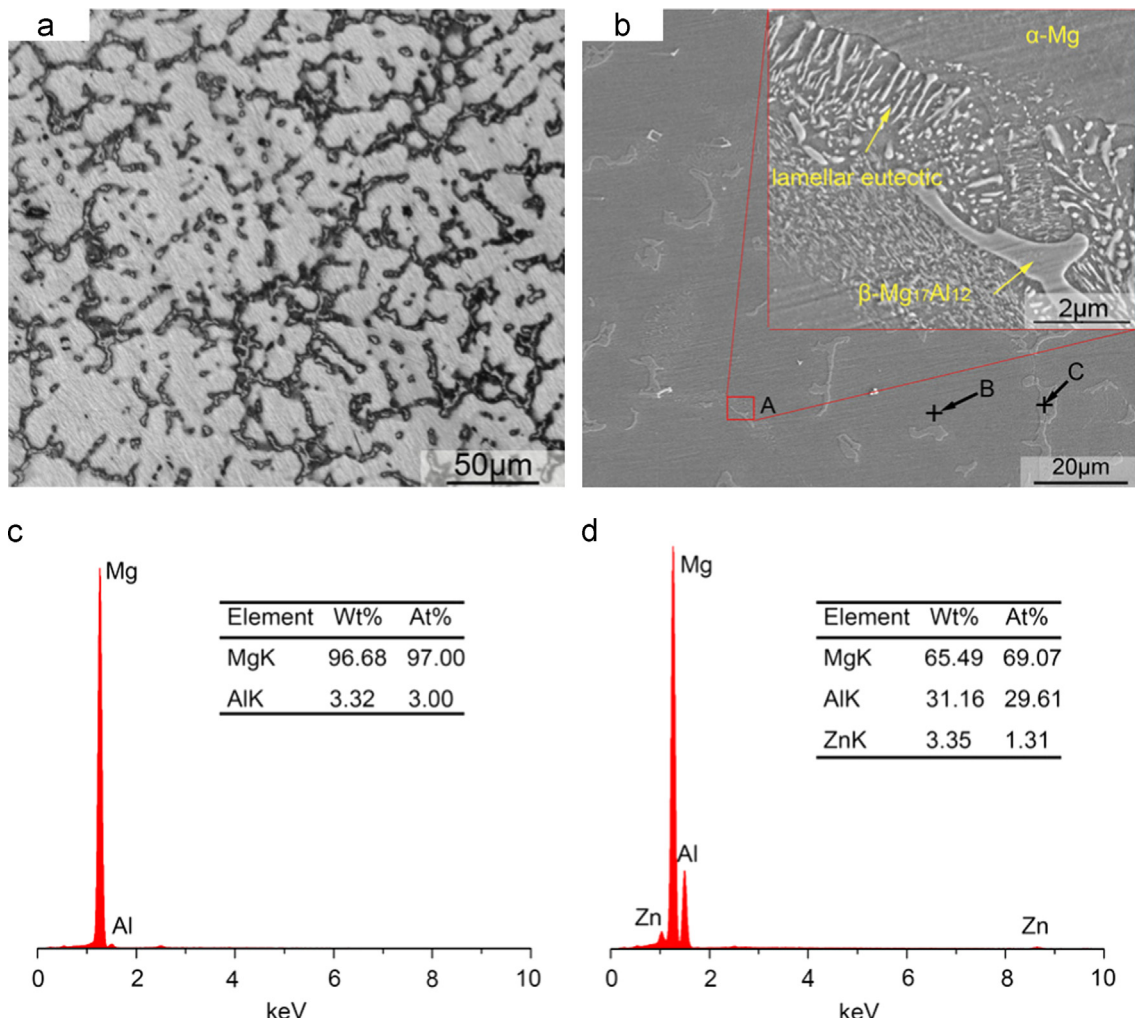


Fig. 8. (a) Optical image and (b) SEM image of the die-cast AZ91D ingot, (c) EDS result of position B in (b), (d) EDS result of position C in (b).

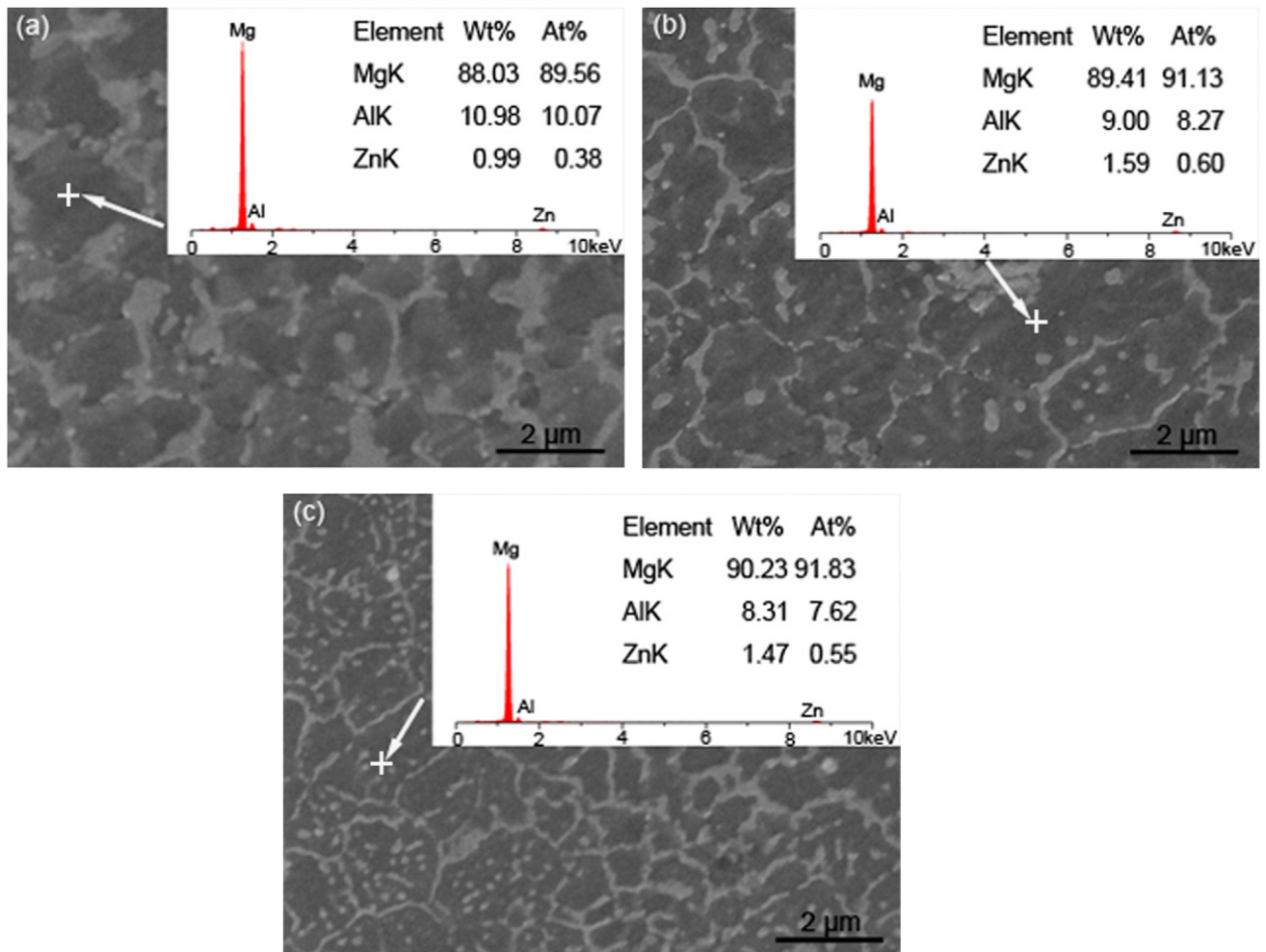


Fig. 9. EDS results of α -Mg matrix of the SLMed AZ91D deposited at E_v of (a) 166.7 J/mm³, (b) 111.1 J/mm³ and (c) 83.3 J/mm³.

cooling rate results in the more divorced structure. Therefore, change in the form of β phase between SLMed and die-cast AZ91D is induced by the high cooling rate inherent to SLM process.

For the die-cast sample, most of the Al and Zn elements concentrate in the β -Mg₁₇Al₁₂ phase, as shown in Fig. 8c and d. The decrease of Al content in α -Mg solid solution not only reduces the effect of solution strengthening but also deteriorates the corrosion behavior [21]. Therefore, element distribution of the SLMed AZ91D is also necessary to be evaluated. Fig. 9 presents EDS results of the α -Mg solid solution of the SLMed samples at different energy inputs. The concentration of Al element in the α -Mg solid solution is much higher than that of the die-cast sample. It could be observed that Al content in the α -Mg matrix decreases from 10.98 wt% to 8.31 wt% with decreasing energy input, which is in accord with the XRD peak shifting shown in Fig. 5. Along with the decrease in energy input, the effect of "solute capture" becomes stronger whilst burning loss rate of Mg atoms reduces. Therefore, under the interaction between "solute capture" and element evaporation, Al concentration in the α -Mg decreases with the decreasing energy input in spite of the fact that more proportion of Al atoms are captured. Fig. 10 compares the dispersion of Mg and Al elements in the AZ91D sample deposited at 166.7 J/mm³ and the die-cast AZ91D ingot sample. It could be found that distributions of Mg and Al are much more uniform in the deposited AZ91D and there is no distinct variation in element contents between OLR and CST. Moreover, the distributions of Mg and Al in deposited samples at other energy inputs are similar

with the result shown in Fig. 10 though they are not given here to save space.

Composition homogenization of the deposited AZ91D should be decided by the solidification procedure during SLM. Firstly, the difference of composition between supersaturated α -Mg and β -Mg₁₇Al₁₂ is diminished by the effect of "solute capture". Secondly, convection in the molten pool helps to homogenize the liquid. According to fluid flow model proposed by He et al. [22], driving force for liquid convection in the molten pool produced by laser irradiation consists of buoyancy and Marangoni force. Which one dominates the convection process can be evaluated from the ratio of surface-tension Reynolds number (Ma) to buoyancy-related Grashof number (Gr):

$$R_{s/b} = \frac{Ma}{Gr} = \frac{L_R |\partial\gamma/\partial T|}{g\rho\delta L_b^3} \quad (3)$$

where L_R is the pool radius taken as half of the width of scanning track, $\partial\gamma/\partial T$ is the temperature coefficient of surface tension, g is the gravitational acceleration, ρ is the density of materials, δ is the thermal expansion coefficient and L_b is the characteristic length for the buoyancy force which is approximately one eighth of the width of scanning track. Take the sample fabricated at 166.7 J/mm³, according to the average width of the scanning track 108 μm measured from Fig. 6 and physical properties of AZ91D recorded in the literature [23], $R_{s/b}$ is about 7.20×10^7 . Thus, fluid flow in the molten pool is mainly driven by Marangoni convection. The maximum liquid velocity in the molten pool is believed to

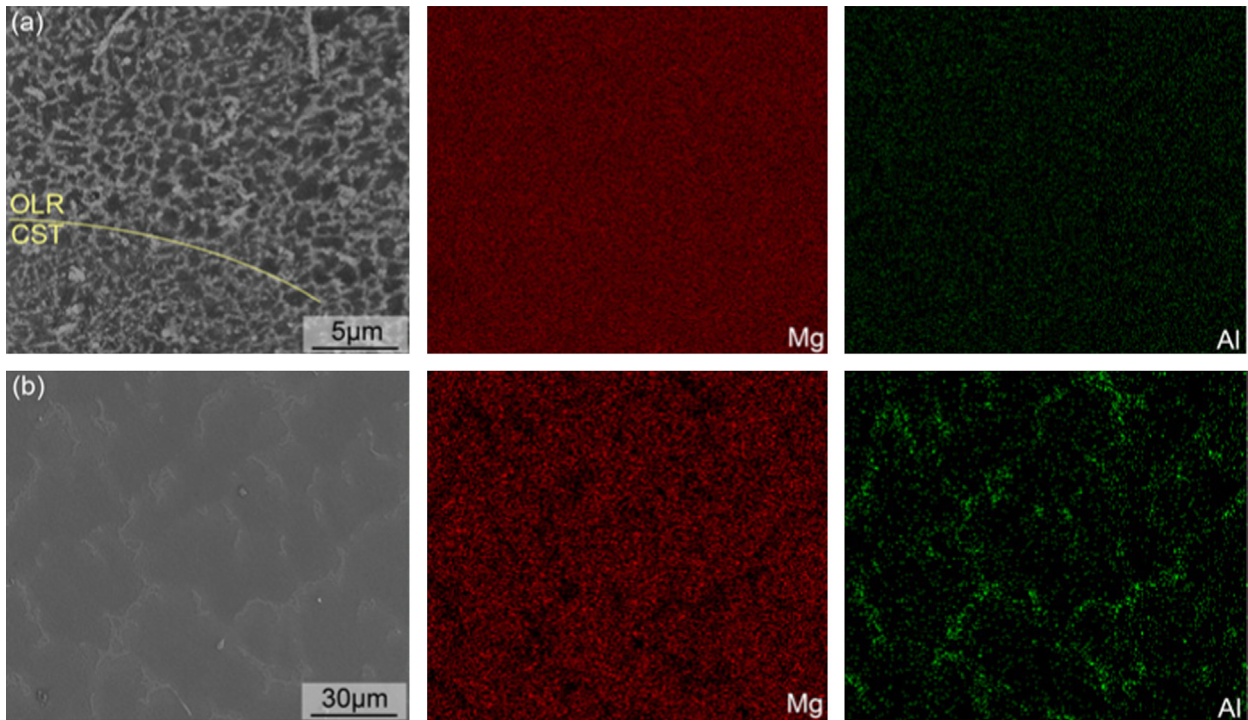


Fig. 10. EDS images of (a) the SLMed AZ91D at E_v of 166.7 J/mm^3 and (b) the die-cast AZ91D.

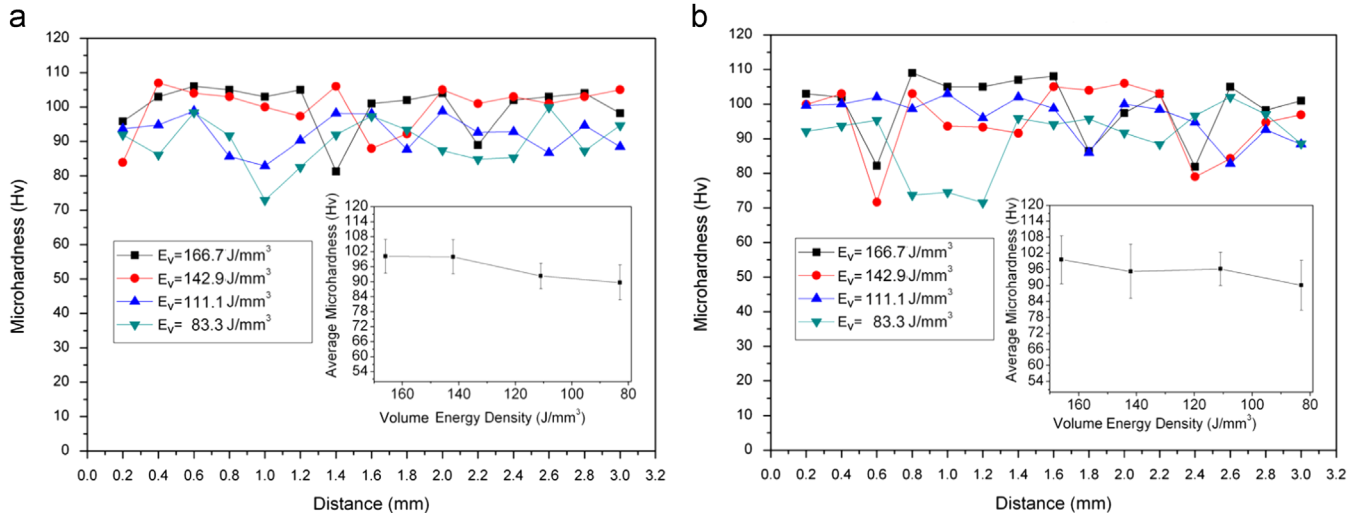


Fig. 11. Microhardness of SLMed AZ91D samples on cross section (a) and vertical section (b).

be positive correlation with the temperature gradient [24]. Due to the Gaussian distribution of incident laser and small size pool inherent to SLM technology, a high temperature gradient between the center and edge of the molten pool is generated, which results in a strong Marangoni convection to improve the homogeneous dispersion of Mg and Al elements.

3.3. Mechanical properties

Fig. 11 presents the microhardness on two sections for AZ91D samples deposited at several representative E_v chosen in zone B of the processing map. Due to the variation in microstructure between OLR and CST, the microhardness fluctuates in a small range on both sections for all tested samples. However, the microhardness of deposited samples shows directional independence. The average microhardness of SLMed samples ranges from 85 to 100 HV, which is much higher than that of the commercial

die-cast ingot (58 HV). Considering the SLMed AZ91D sample built at 166.7 J/mm^3 , the improvement of microhardness should be ascribed to the following reasons.

First, according to the Hall-Petch formula [25], grain refinement can significantly increase the microhardness of magnesium alloys. Due to the variation of grain size between CST and OLR, the average grain size $d_{\alpha-SLM}$ of α -Mg matrix can be evaluated to be $1.2 \mu\text{m}$ using the area-based averaging method [26]:

$$d_{\alpha-SLM} = [f_{CST}/d_{\alpha-CST}^2 + (1-f_{CST})/d_{\alpha-OLR}^2]^{-1/2} \quad (4)$$

where f_{CST} is area fraction of CST (measured as 65% from Fig. 6d), $d_{\alpha-CST}$ ($1.0 \mu\text{m}$) and $d_{\alpha-OLR}$ ($2.9 \mu\text{m}$) are the average size of α -Mg in CST and OLR respectively. Meanwhile, the average grain size of α -Mg in the die-cast sample is measured as $57 \mu\text{m}$. Therefore, grain refinement helps to improve the microhardness of the SLMed AZ91D.

Second, Al concentration in α -Mg of the SLMed sample is much higher than that of the die-cast AZ91D due to the effect of “solute capture”. According to the theory of solid solution strengthening, a higher solid solubility would induce superior mechanical strengths [27]. For Mg-Al alloys, the variation in microhardness is in proportion to the Al content in α -Mg [28]. Therefore, solid solution strengthening also contributes to the high microhardness of the SLMed AZ91D.

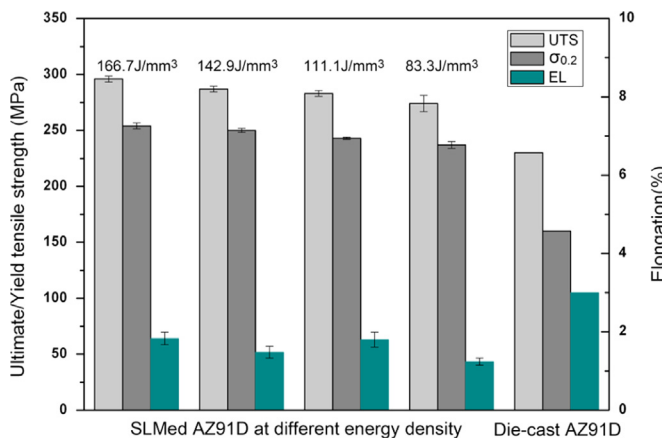


Fig. 12. Tensile performance of samples deposited at different E_v and that of the die-cast AZ91D.

In addition, the hard-brittle β phase can be considered as a strengthening phase when distributing in the soft α -Mg matrix. According to Yang's and Yim's reports [29,30], higher fraction of the strengthening phase would result in the improvement of strength and microhardness. Here, based on the area-based averaging theory [26] and Figs. 7c, d and 8a, the fraction of β phase in the SLMed AZ91D is determined to be 31.7% whilst that of the die-cast AZ91D is 36.2%. Thus, it can be concluded that β phase does not contribute to the improvement of microhardness for the SLMed AZ91D samples.

Under the interaction of “solute capture” and element evaporation, the content of hard-brittle β phase and the solid solubility of solute elements in α -Mg matrix decrease simultaneously with decreasing E_v . Meanwhile, there is no significant difference on the average grain sizes of α -Mg in different SLMed samples. Therefore, the microhardness becomes lower gradually when E_v decreases from $166.7 J/mm^3$ to $83.3 J/mm^3$, as shown in Fig. 11.

Fig. 12 summarizes the tensile properties of samples deposited at those above-mentioned E_v . For comparison, the tensile properties of the die-cast AZ91D (according to ASTM standard B94-07) are also included. Ultimate strength (UTS) and yield strength ($\sigma_{0.2}$) of the SLMed samples are superior to those of the die-cast AZ91D alloy though their elongation (EL) has a slight drop from 3% to 1.24–1.83%. It is apparent that laser energy input can also influence the tensile properties. In Fig. 12, the average UTS and $\sigma_{0.2}$ of the SLMed samples, decrease gradually from 296 MPa and 254 MPa at $166.7 J/mm^3$ to 274 MPa and 237 MPa at $83.3 J/mm^3$. This variation should be first ascribed to the poor relative densities of the SLMed

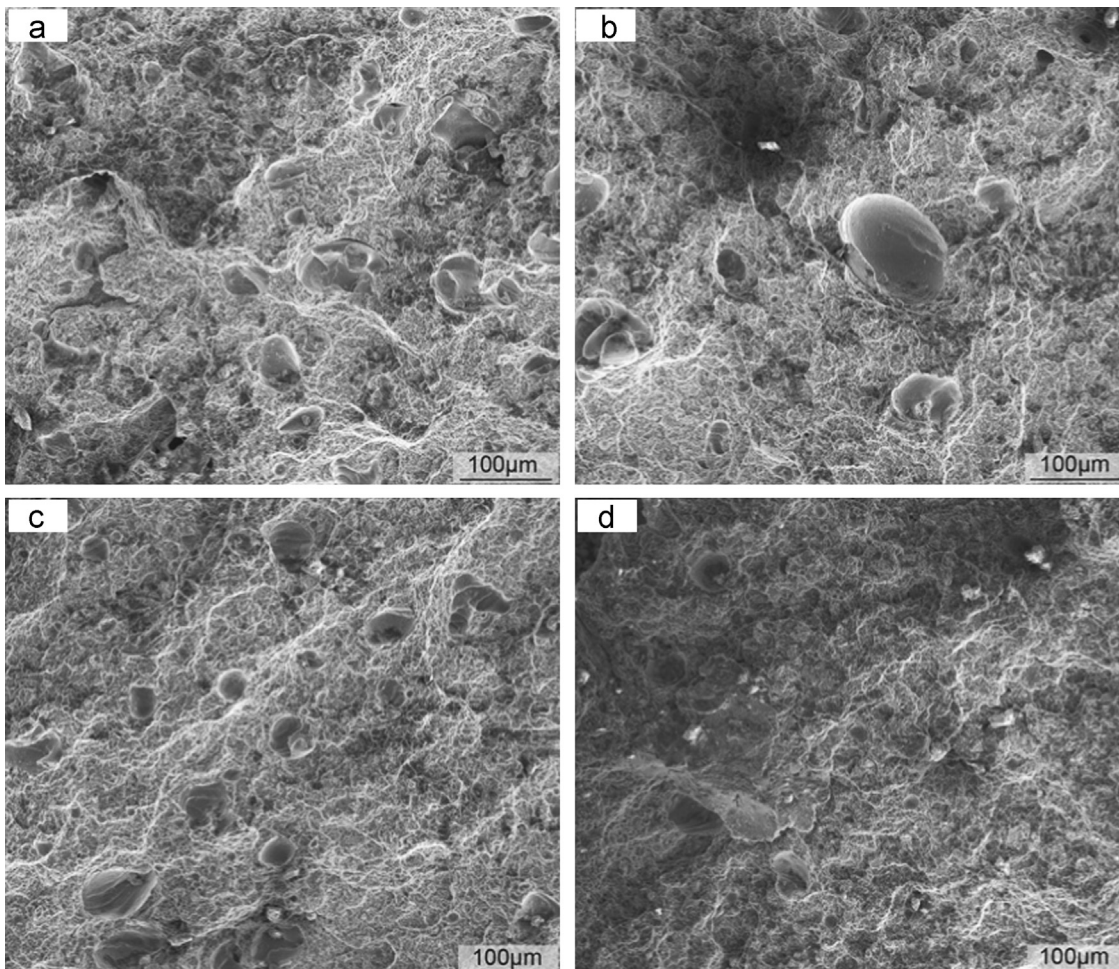


Fig. 13. Fracture morphologies of SLMed tensile samples at different E_v . (a) $166.7 J/mm^3$, (b) $142.9 J/mm^3$, (c) $111.1 J/mm^3$, (d) $83.3 J/mm^3$.

samples obtained at lower energy inputs. Another factor that cannot be ignored to degrade the tensile properties is the lower solid solubility of the α -Mg matrix and smaller quantity of the intermetallic β phase induced by lower energy inputs.

The fracture morphologies of tensile samples were also observed, as shown in Fig. 13. All the tensile samples exhibit the feature of ductile–brittle hybrid fracture for bestrewing dimples and ductile tearing ridges together with quasi-cleavages. This kind of fracture mode should be related to the multiple-phase microstructures and the micropores distributing in the samples. Soft α -Mg matrix results in the ductile feature whereas brittle β phase and the micropores reduce ductility by stress concentration and lead to the formation of cleavage-like brittle characteristics.

4. Conclusions

Selective laser melting of AZ91D has been carried out in this study. Effect of laser energy input on the formability, microstructure and mechanical properties of the SLMed AZ91D samples are analyzed. The major findings are listed as follows:

- (1) Formation qualities of the as-deposited AZ91D samples depend on the laser energy inputs during SLM process. There is a proper processing window to fabricate AZ91D powders, where high density AZ91D without obvious macro-defects can be obtained between 83 J/mm³ and 167 J/mm³. Samples are unable to be deposited at laser energy inputs higher than 214 J/mm³ due to intense evaporation, whereas the fabricated samples are loosened at laser energy inputs below 77 J/mm³ due to “balling effect” and incomplete melt of powders.
- (2) All the deposited AZ91D samples show a layerwise feature with neighbor tracks and layers stacking close together. In microstructure, the SLMed AZ91D consists of equiaxed α -Mg matrix and fully divorced eutectic β -Mg₁₇Al₁₂. The average size of α -Mg in OLR is a little larger than that in CST due to the remelting process though the element contents are quite uniform. Due to the interaction of “solute capture” and element evaporation, the content of hard-brittle β phase and solubility of solute elements in α -Mg matrix decrease simultaneously with decreasing laser energy inputs.
- (3) The microhardness of all samples shows directional independence. There is a fluctuation of microhardness within a narrow range on both sections for all tested samples. The microhardness and tensile strengths of the SLMed AZ91D at room temperature are superior to those of the die-cast AZ91D. Grain refinement and solid solution strengthening are the main strengthening mechanisms for SLMed AZ91D.
- (4) In this study, nearly full dense AZ91D (99.52%) with the microhardness of 100 Hv, UTS of 296 MPa and $\sigma_{0.2}$ of

254 MPa can be obtained using laser volume energy density of 166.7 J/mm³.

Acknowledgment

This work is supported by the National Natural Science Foundation of China through Program no. 51075164 and the Fundamental Research Funds for the Central Universities through Program no. HUST-2014QT006.

References

- [1] B.L. Mordike, T. Ebert, Mater. Sci. Eng. A 302 (2001) 37–45.
- [2] F.H. Froes, D. Eliezer, E. Aghion, J. Miner. Met. Mater. Soc. 50 (1998) 30–34.
- [3] C.K. Seal, K. Vince, M.A. Hodgson, IOP Conf. Ser. Mater. Sci. Eng. 4 (2009) 012011.
- [4] M.P. Staiger, A.M. Pietak, J. Huadmai, G. Dias, Biomaterials 27 (2006) 1728–1734.
- [5] M.K. Kulekci, Int. J. Adv. Manuf. Technol. 39 (2008) 851–865.
- [6] E. Aghion, N. Moscovitch, A. Arnon, Mater. Sci. Eng. A 447 (2007) 341–346.
- [7] I. Yadroitsev, A. Gusarov, I. Yadroitseva, I. Smurov, J. Mater. Process. Technol. 210 (2010) 1624–1631.
- [8] I. Yadroitsev, P. Krakhmalev, I. Yadroitseva, S. Johansson, I. Smurov, J. Mater. Process. Technol. 213 (2013) 606–613.
- [9] T. Vilaro, C. Colin, J.D. Bartout, Metall. Mater. Trans. A 42A (2011) 3190–3199.
- [10] L. Wang, S. Felicelli, Y. Gooroochurn, P.T. Wang, M.F. Horstemeyer, Mater. Sci. Eng. A 474 (2008) 148–156.
- [11] C.C. Ng, M. Savalani, H.C. Man, Rapid Prototyping J. 17 (2011) 479–490.
- [12] B.C. Zhang, H.L. Liao, C. Coddet, Mater. Des. 34 (2012) 753–758.
- [13] Z.M. Wang, K. Guan, M. Gao, X.Y. Li, X.F. Chen, X.Y. Zeng, J. Alloys Compd. 513 (2012) 518–523.
- [14] K. Guan, Z.M. Wang, M. Gao, X.Y. Li, X.Y. Zeng, Mater. Des. 50 (2013) 581–586.
- [15] D. Min, J. Shen, S.Q. Lai, J. Chen, N. Xu, H. Liu, Opt. Lasers Eng. 49 (2011) 89–96.
- [16] C.H. Suresh, N. Koga, J. Phys. Chem. A 105 (2001) 5940–5944.
- [17] Y.C. Guan, W. Zhou, Z.L. Li, H.Y. Zheng, Appl. Surf. Sci. 255 (2009) 8235–8238.
- [18] M.J. Aziz, J. Appl. Phys. 53 (1982) 1158–1168.
- [19] K.N. Braszczyńska-Malik, J. Alloys Compd. 477 (2009) 870–876.
- [20] A.K. Dahle, Y.C. Lee, M.D. Nave, P.L. Schaffer, D.H. StJohn, J. Light Met. 1 (2001) 61–72.
- [21] Z.H. Wen, C.J. Wu, C.S. Dai, F.X. Yang, J. Alloys Compd. 488 (2009) 392–399.
- [22] X. He, J.W. Elmer, T. DebRoy, J. Appl. Phys. 97 (2005) 084909.
- [23] K. Abderrazak, S. Bannour, H. Mhiri, G. Lepalec, M. Autric, Comput. Mater. Sci. 44 (2009) 858–866.
- [24] D. Höche, S. Müller, G. Rapin, M. Shinn, E. Remdt, M. Gubisch, P. Schaaf, Metall. Mater. Trans. B 40 (2009) 497–507.
- [25] N. Xu, J. Shen, W.D. Xie, L.Z. Wang, D. Wang, D. Min, Mater. Charact. 61 (2010) 713–719.
- [26] W.Z. Chen, Y. Yu, X. Wang, E.D. Wang, Z.Y. Liu, Mater. Sci. Eng. A 575 (2013) 136–143.
- [27] H.M. Wen, T.D. Topping, D. Isheim, D.N. Seidman, E.J. Lavernia, Acta Mater. 61 (2013) 2769–2782.
- [28] C.H. Cáceres, D.M. Rovera, J. Light Met. 1 (2001) 151–156.
- [29] Y. Yang, X.D. Peng, H.M. Wen, B.L. Zheng, Y.Z. Zhou, W.D. Xie, E.J. Lavernia, Metall. Mater. Trans. A 44A (2013) 1101–1113.
- [30] C.D. Yim, K.S. Shin, Mater. Sci. Eng. A 395 (2005) 226–232.